

Supporting Information

Role of cooperative interactions in the intercalation of hetero-atoms between graphene and a metal substrate

Geng Li,^{†#} Haitao Zhou,^{†#} Lida Pan,^{†#} Yi Zhang,[†] Li Huang,[†] Wenyan Xu,[†] Shixuan Du,[†] Min Ouyang,[‡] Andrea C. Ferrari,^{§*} and Hong-Jun Gao^{†*}

[†]*Institute of Physics, Chinese Academy of Sciences, Beijing 100190, PR China*

[‡]*Department of Physics and Center for Nanophysics and Advanced Materials, University of Maryland, College Park, MD 20742, USA*

[§]*Cambridge Graphene Centre, University of Cambridge, Cambridge, CB3 0FA, UK*

Contents

1. STM images of SLG on Ru(0001)
2. Raman spectrum of SLG/Si/Ru(0001)
3. Si cluster aggregation on the SLG/Ru surface with different temperatures
4. Point defects induced by Si at 400 °C
5. Defect formation due to interaction between Si, graphene and substrate
6. Relation between defect density and Si intercalation efficiency
7. High-resolution STM images of graphene on Ru(0001) after Ar⁺ ion bombardment
8. Ab initio calculations of energy barrier for the Si intercalation

1. STM images of SLG on Ru(0001)

Graphene is grown by ethylene decomposition on a hot Ru(0001) surface.¹ The typical temperature is 1300 K, for a ethylene background pressure of 1×10^{-6} mbar. Fig.S1a shows the ordered moiré structure of a typical single layer graphene (SLG) grown on Ru. A high-resolution image is in Fig.S1b. Three regions are distinguished by red (atop site), blue (fcc site) and green (hcp site) dots, respectively.¹⁻³ A typical value of surface corrugation along z-direction is ~ 0.1 nm.

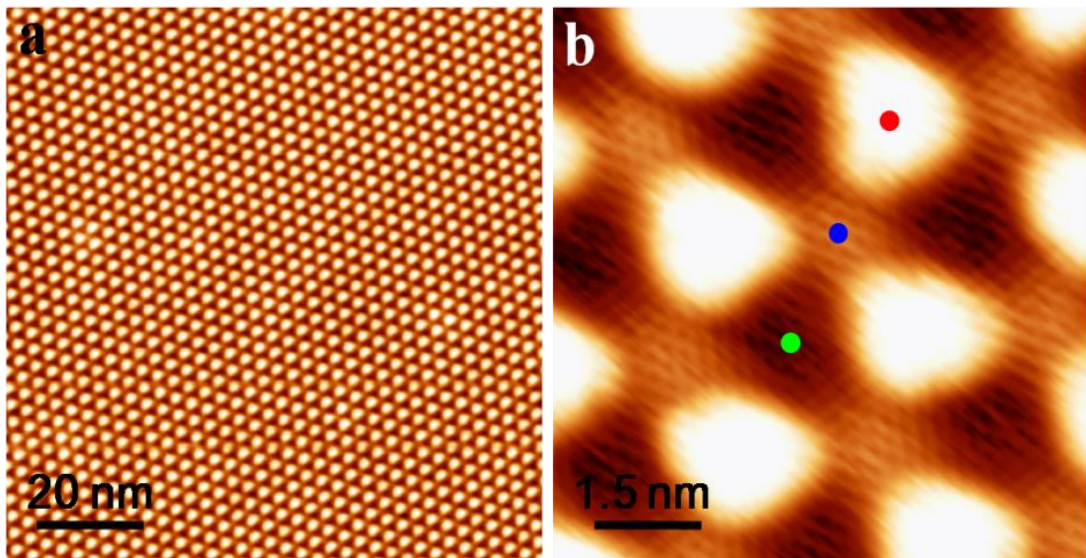


Figure S1. STM topography of SLG/Ru moiré structure. (a) Large-scale STM image showing perfect G/Ru surface. (b) High-resolution image showing detailed structure of the moiré pattern.

2. Raman spectrum of SLG/Si/Ru(0001)

The Raman spectrum of SLG/Ru(0001) after intercalation of a full Si layer is shown in Fig. S2. The spectrum is measured with a HORIBA HR800, spectrometer, with a power on the sample below 1 mW at 532 nm. SLG/Ru(0001) shows a negligible signal due to the strong coupling between graphene and the substrate.⁴ After intercalation, the G peak and 2D peak appear. Their position and intensity ratio⁵⁻⁸ are indicative of a significant doping, consistent with previous ARPES and STS data.⁹ The absence of a significant D peak indicates a small amount of defects.^{8,10,11}

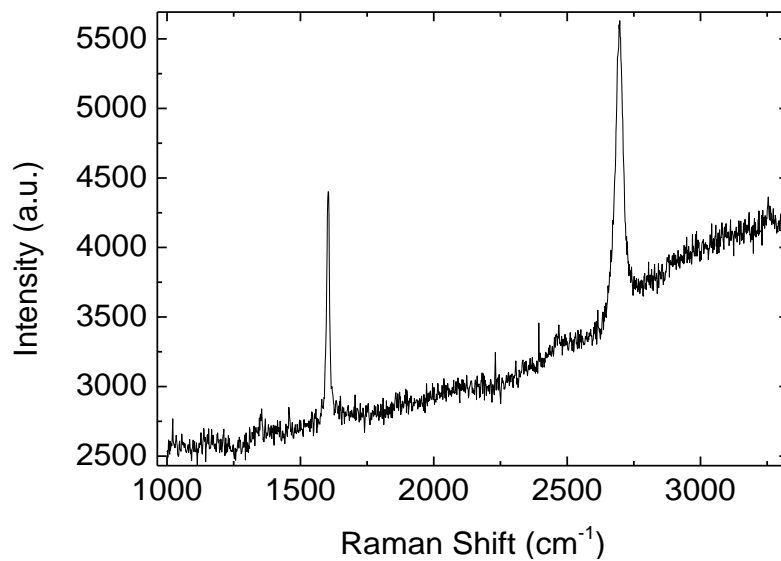


Figure S2. Raman spectrum of SLG/Si/Ru(0001).

3. Si cluster aggregation on the SLG/Ru surface at different temperatures

Figure S3a-c show 0.05 monolayer (ML) Si on a SLG/Ru surface, followed by annealing at 25, 300 and 350 °C. Si clusters aggregate to larger sizes for increasing annealing temperature. The average cluster size increases from 2 to 4 nm after annealing at 300 and 350 °C, respectively.

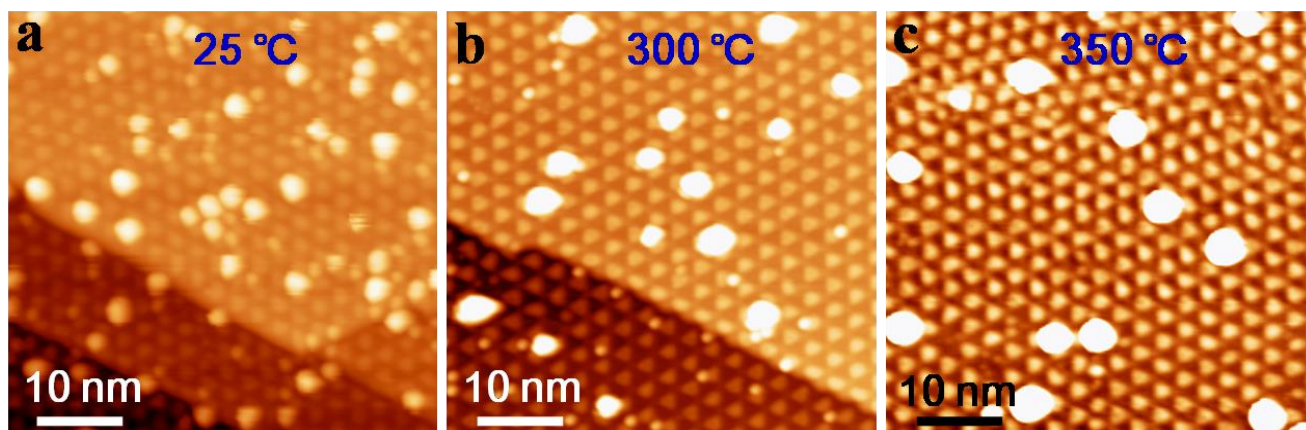


Figure S3. STM images of Si clusters aggregated on the SLG/Ru surface.

4. Point defects induced by Si at 400 °C

Figs. S4a,b show two enlarged images of Fig.2a. The small bright spots highlighted by the blue solid arrows can be assigned to point defects induced by Si adatoms at 400 °C, as discussed in the main text. There are some brighter spots (highlighted by green dashed arrows), as shown in Fig. S4b. They are usually fuzzy in STM images and are attributed to several Si adatoms trapped at the defect sites. The formation of the defects is reproducible, however, the experimental conditions are hard to control since various kinetic processes, such as Si surface diffusion, defect formation and repairing compete at 400 °C. We find that a moderate amount of Si (< 0.1 ML), and an annealing temperature between 350 and 400 °C for ~ 10 min, followed by fast sample cooling (~ 15 min) are critical in order to observe these defects.

Figs. S4c shows a control experiment by heating SLG/Ru under the same condition as Fig. S4a,b but without pre-deposition of Si. No vacancy defects are observed.

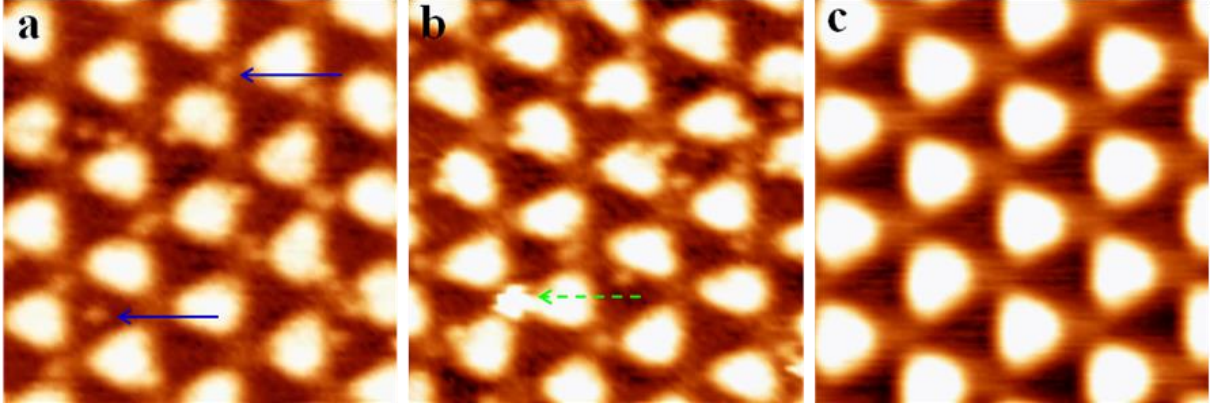


Figure S4. Defects induced by Si adsorption. (a) and (b) Zoom-in STM images of Fig. 2a, $10 \text{ nm} \times 10 \text{ nm}$. Solid and dashed arrows outline point defects and Si adatoms on defect sites, respectively. (c) $10 \text{ nm} \times 10 \text{ nm}$ SLG/Ru after annealing under same conditions as Figure S4a and b.

5. Defect formation due to interaction between Si, graphene and substrate

The relation between formation energy, Si and Ru is schematically shown in Fig. S5. Both the Si adatoms and the Ru substrate contribute to the decrease of the defect formation energy.

Density functional theory (DFT) calculations are performed within the local density approximation (LDA),¹² using the Vienna *ab-initio* simulation package (VASP).¹³ The projector augmented wave (PAW)¹⁴ method is used. The electronic wave functions are expanded in plane waves with a kinetic energy cutoff of 400 eV. The structures are relaxed until residual forces are smaller than $0.01 \text{ eV}/\text{\AA}$. A $\sim 13 \text{ \AA}$ vacuum layer is applied in the direction perpendicular to the substrate to avoid the interaction between neighboring supercells. The system is modeled by a Ru(0001) slab consisting of 2 layers of Ru atoms. A compressed 5×5 Ru(0001) substrate is used in order to fit a 5×5 graphene supercell, and the Ru substrate atoms are kept fixed in order to reduce the computational cost. The defect formation energy is defined¹⁵ as

$$E_{vac} = E_{graphene_v} + E_{carbon} - E_{graphene}, \quad (1)$$

$$E_{vac_Ru} = E_{Si/graphene_v/Ru} + E_{carbon} - E_{Si/graphene/Ru}, \quad (2)$$

E_{vac} and E_{vac_Ru} represent the defect formation energies of free standing SLG and of SLG on Ru.

$E_{graphene}$ is the total energy of free standing SLG, and $E_{graphene_v}$ is the total energy of free standing SLG with a single atomic vacancy. E_{carbon} is the energy per single carbon atom in free-standing SLG.

$E_{Si/graphene/Ru}$ is the total energy of the Si adatoms on SLG on Ru. $E_{Si/graphene_v/Ru}$ is the total energy of the Si adatom on top of defected graphene on a Ru substrate.

A similar approach is applied for calculations of systems with other hetero-atoms and substrates, as for Fig. S10e.

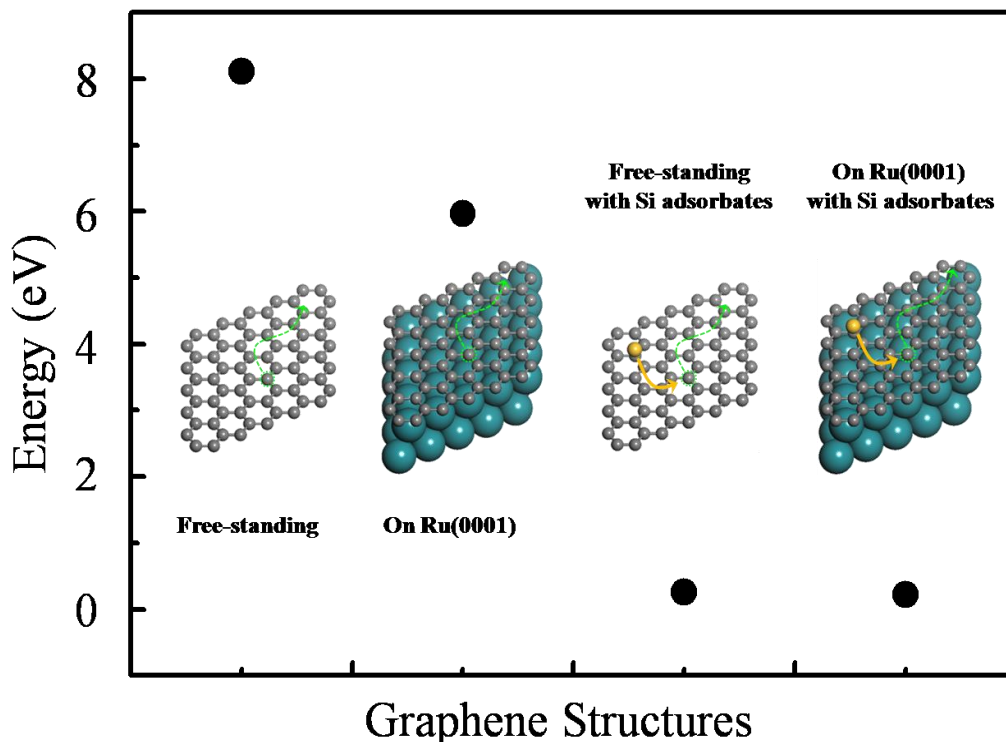


Figure S5. Ab initio calculations of formation energy of graphene defects with three different structures. From left to right, free-standing SLG, SLG on Ru(0001), free-standing SLG with Si adsorbates, and SLG on Ru(0001) with Si adsorbates. Both the Si adsorbates and the Ru substrate can decrease the defect formation energy from 8.09 eV to 5.97 eV, 0.26 eV and 0.23 eV, respectively.

6. Relation between defect density and Si intercalation efficiency

Even though a step-wise mechanism is proposed (Fig. 1d), the different intercalation stages are dynamically inter-correlated and can happen simultaneously. As a result, the diffusion process of the Si atoms and the opening of carbon vacancies by the cooperative effect are hard to separate and characterize. Therefore, in order to confirm the role of the carbon vacancies in the Si diffusion process, as well as the relation between defect density and intercalation efficiency, we prepared samples with carbon vacancies by using Ar^+ ion bombardment. Low energy (80-100 eV) ion bombardment can create vacancies in graphite or graphene.¹⁶⁻¹⁹ The threshold energy to remove a carbon atom from the graphite surface is ~ 40 eV^{16,17} and it is possible to use up to 140 eV to create single vacancies on a

graphene surface^{18,19} without severe damage to the graphene surface. We use an Omicron ISE 10 ion source with applied voltage adjusted between 0 and 5000 V. We find that 80-100 eV can create single vacancy defects, as shown in Fig. S6. The density of defects is determined by ion energy, base pressure, filament emission current as well as bombardment time. In our experiments, we fix the ion energy at 100 eV, the Ar pressure at 3×10^{-6} mbar and the emission current at 0.1 mA. We then vary the irradiation time to tune the defect density.

Figs. S6a-c show three SLG/Ru surfaces after 60, 90 and 120 min irradiation. The small bright spots highlighted by the green arrows are point defects, and the larger white protrusions in Figure S6c are Ar bubbles¹⁶ at the SLG/Ru interface, as explained in Section S7. Then we deposit equal amounts (~ 2 ML) of Si onto these three samples and let anneal them under the same conditions (700 °C for 30 min). Figs. S6d-f are the STM topographies of these samples after Si intercalation under the same conditions (700 °C for 30 min). The higher the defect density, the more Si can be intercalated. The observation suggests that the existence of defects promotes the intercalation process.

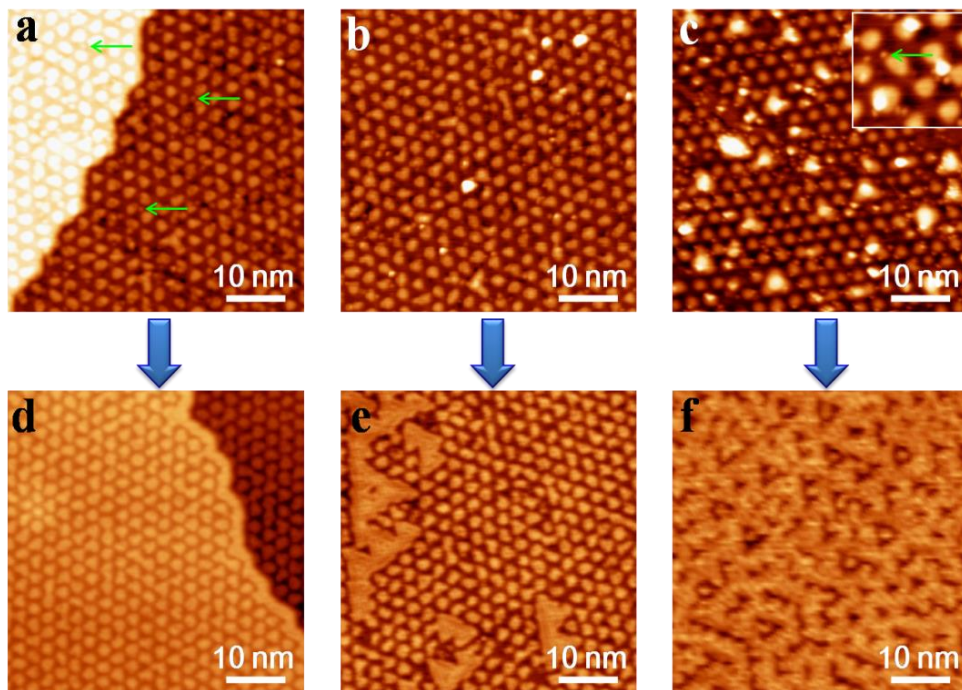


Figure S6. STM images of SLG on Ru(0001) with defects created by ion bombardment. SLG/Ru samples are exposed to low energy Ar^+ ions for (a) 60 min, (b) 90 min and (c) 120 min. Inset in (c): 10 nm \times 10 nm image showing point defects. (d)-(f) Si intercalated SLG/Ru obtained by depositing Si on the samples in (a-c). All samples are prepared with the same Si intercalation parameters: room temperature deposition of ~ 2 Si MLs, followed by annealing at 700 °C.

7. High-resolution STM images of graphene on Ru(0001) after Ar⁺ ion bombardment

To illustrate the effect of Ar⁺ ion bombardment on graphene, we consider a sample where SLG and bi-layer graphene (BLG) coexist. Figs S7a,b show high-resolution images of point defects (blue arrows) as well as Ar bubbles¹⁶ (white dashed arrows). The point defects are mostly single vacancies, and their typical triangular pattern²⁰ can be seen on the BLG areas, where the uppermost graphene film is near free-standing (Figs S7c,d). The ions can also penetrate the SLG/Ru interface, leading to formation of bright bubbles on the surface¹⁶, as shown in Figures S6b,c and S7a,b.

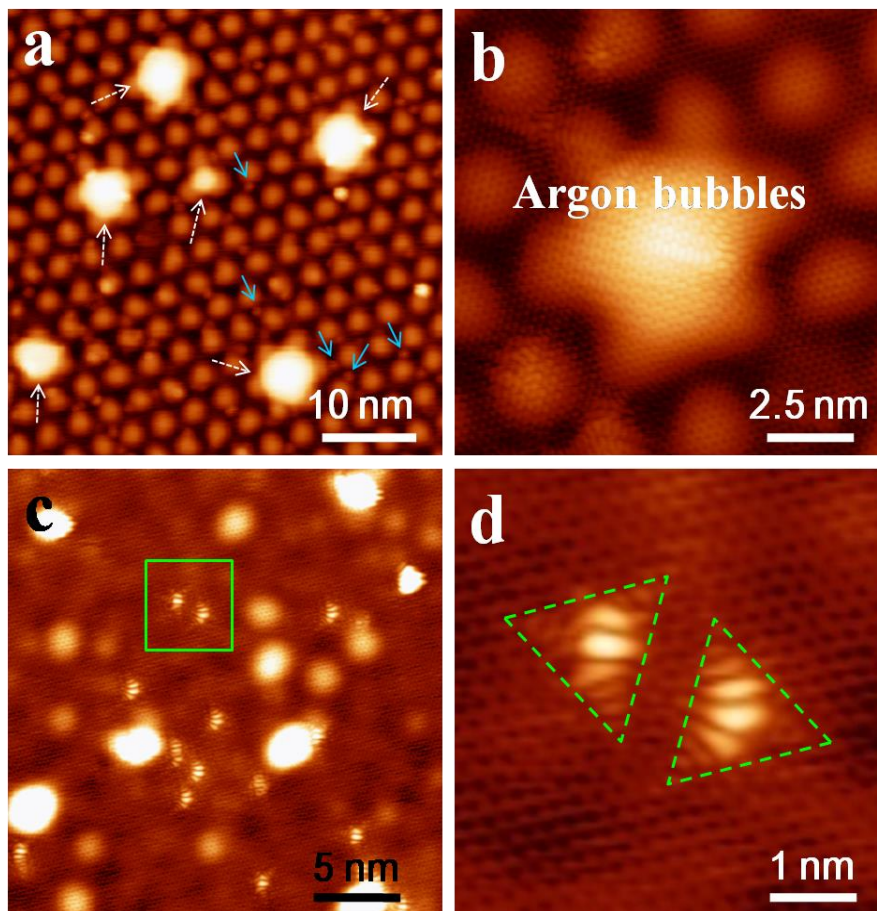


Figure S7. STM images of ion bombarded graphene/Ru(0001) surfaces. (a) and (b) SLG after bombardment showing both point defects (blue arrows) and Ar bubbles (white dashed arrows). (c) BLG on Ru(0001) after Ar ion bombardment (sample bias $V_s = -1.0$ V, tunneling current $I_t = 0.5$ nA). (d) Zoom-in image of the green square in (c). Typical single vacancy defects can be identified as outlined by green triangles.

8. Ab initio calculations of energy barrier for Si intercalation

The surface is modeled by a Ru(0001) slab consisting of two layers of atoms, cleaved from bulk

Ru (lattice constants: $a=2.68 \text{ \AA}$, $c=4.2233 \text{ \AA}$). A 9% compression of the 5×5 Ru(0001) substrate is used in order to fit the 5×5 graphene supercell, and the atoms of Ru(0001) are fixed in order to reduce the computational cost. A $\sim 15 \text{ \AA}$ vacuum layer is applied in the direction perpendicular to the Ru(0001) substrate to avoid interaction between neighboring supercells. The structures are relaxed until residual forces are smaller than 0.01 eV/\AA . The intercalation process is simulated using the climb Nudged Elastic Band method,²¹ with linear interpolation between initial and final states. Eight intermediate states are constructed by using linear interpolation. For SLG without defects, the calculated barrier is 6.13 eV . When a single vacancy is present, the barrier reduces to 0.66 eV . If the Ru substrate is further considered, the barrier becomes 0.33 eV and the existence of Ru also contributes to the total energy reduction in the final state (Fig. 2e). Direct comparison between calculated energy barriers and our experimental values (such as thermal energy) might be challenging because of simplifications when compared with realistic materials system. E.g., changing Ru substrate thickness may change the calculated energy barriers. In addition, the size of the hetero-atom clusters might have an effect. Furthermore, we take a simplified model (5×5 graphene supercell) here to reveal the cooperative effects of defects and substrate during intercalation, which may also cause a difference in energy barrier compared with experiments. A supercell without strain should also be necessary. E.g., a 12×12 graphene on a 11×11 Ru(0001), or even bigger, 25×25 graphene on 23×23 Ru(0001) were observed in experiments.²² These supercells have 576 atoms and 2308 atoms, respectively, even if we only consider two layers of Ru(0001). Taking fully into account all these effects requires substantial computation resources. Nevertheless, our current calculation agrees qualitatively with experiments.

We also calculated the diffusion barrier of Si atoms on Ru, which is less than 0.5 eV . This suggests that Si atoms can diffuse and form bonds with other Si at the interface under our experimental conditions. When the dangling bonds of Si are saturated by surrounding Si atoms, the bonding between Si and Ru weakens. As a result, the formation of the intercalated Si layer is energetically most favorable. This is consistent with our observations in Fig. 3a, where the interfacial Si atoms can diffuse to the space under the atop sites in the SLG moiré pattern, where the SLG-Ru distance is the largest.

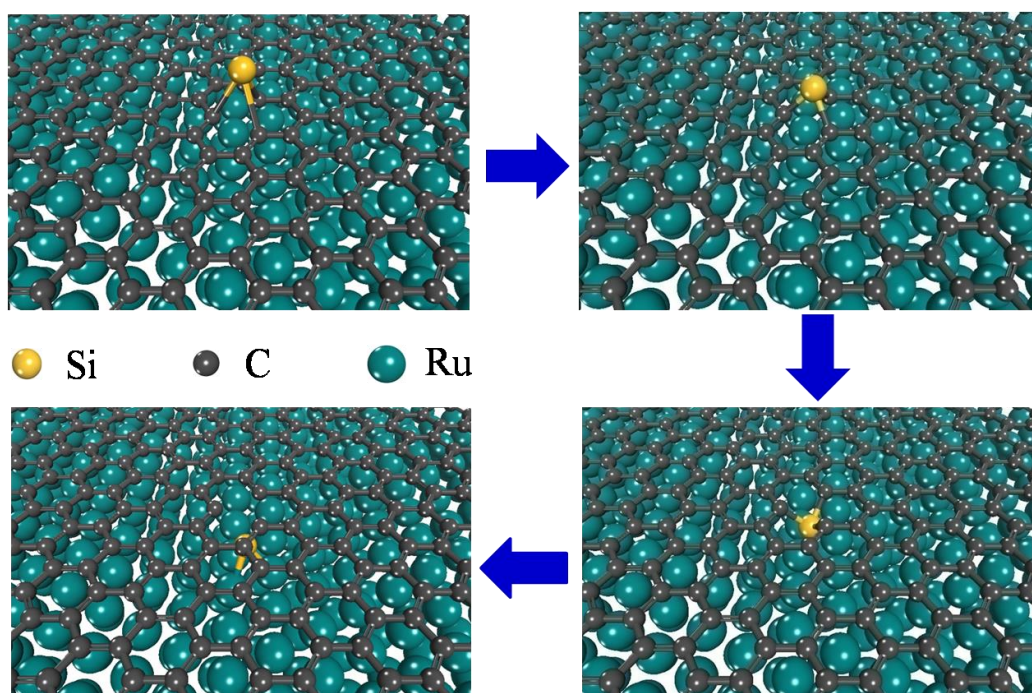


Figure S8 | Ab initio Calculations showing a Si atom penetrating through one-atom vacancies in SLG/Ru(0001).

References

- (1) Pan, Y.; Zhang, H.; Shi, D.; Sun, J.; Du, S.; Liu, F.; Gao, H. *J. Adv. Mater.* **2009**, *21*, 2777-2780.
- (2) Zhou, H. T.; Mao, J. H.; Li, G.; Wang, Y. L.; Feng, X. L.; Du, S. X.; Mullen, K.; Gao, H. *J. Appl. Phys. Lett.* **2011**, *99*, 153101.
- (3) Zhang H. G.; Sun J. T.; Low T.; Zhang L. Z.; Pan Y.; Liu Q.; Mao J. H.; Zhou H. T.; Guo H. M.; Du S. X.; Guinea F.; Gao H. -J. *Phys. Rev. B* **2011**, *84*, 245436.
- (4) Sutter, P. W.; Flege, J.; Sutter, E. A. *Nature Mater.* **2008**, *7*, 406-411.
- (5) Das A.; Pisana S.; Chakraborty B.; Piscanec S.; Saha S. K.; Waghmare U. V.; Novoselov K. S.; Krishnamurthy H. R.; Geim A. K.; Ferrari A. C.; Sood A. K. *Nature Nanotech.* **2008**, *3*, 210-215.
- (6) Pisana S.; Lazzeri M.; Casiraghi C.; Novoselov K. S.; Geim A. K.; Ferrari A. C.; Mauri F. *Nature Mater.* **2007**, *6*, 198-201.
- (7) Basko, D. M.; Piscanec, S.; Ferrari, A. C. *Phys. Rev. B* **2009**, *80*, 165413.
- (8) Ferrari, A. C.; Basko, D. M. *Nature Nanotech.* **2013**, *8*, 235-246.
- (9) Mao, J. H.; Huang, L.; Pan, Y.; Gao, M.; He, J.; Zhou, H.; Guo, H.; Tian, Y.; Zou, Q.; Zhang, L.; Zhang, H.; Wang, Y.; Du, S.; Zhou, X.; Castro Neto, A. H.; Gao, H. *J. Appl. Phys. Lett.* **2012**, *100*, 093101.
- (10) Cançado L. G.; Jorio A.; Martins Ferreira E. H.; Stavale F.; Achete C. A.; Capaz R. B.; Moutinho M. V. O.; Lombardo A.; Kulmala T. S.; Ferrari A. C. *Nano Lett.* **2011**, *11*, 3190-3196.
- (11) Ferrari, A. C.; Robertson, J. *Phys. Rev. B* **2000**, *61*, 14095-14107.
- (12) Perdew, J. P.; Zunger, A. *Phys. Rev. B* **1981**, *23*, 5048-5079.
- (13) Kresse, G.; Furthmüller, J. *Phys. Rev. B* **1996**, *54*, 11169-11186.
- (14) Blochl, P. E. *Phys. Rev. B* **1994**, *50*, 17953-17979.
- (15) Boukhvalov D. W.; Katsnelson M. I. *Appl. Phys. Lett.* **2009**, *95*, 023109.
- (16) Marton D.; Boyd K. J.; Lytle T.; Rabalais J. W. *Phys. Rev. B* **1993**, *48*, 6757-6766.
- (17) Hahn J. R.; Kang H.; Song S.; Jeon I. C. *Phys. Rev. B* **1996**, *53*, R1725-R1728.
- (18) Ugeda M. M.; Brihuega I.; Guinea F.; Gómez-Rodríguez J. M. *Phys. Rev. Lett.* **2010**, *104*, 096804.
- (19) Ugeda M. M.; Fernández-Torre D.; Brihuega I.; Pou P.; Martínez-Galera A. J.; Rubén Pérez; Gómez-Rodríguez J. M.

Phys. Rev. Lett. **2011**, *107*, 116803.

(20) Yazyev, O. V.; Helm, L. *Phys. Rev. B* **2007**, *75*, 125408.

(21) Henkelman, G.; Uberuaga, B. P.; Jonsson, H. A. *J. Chem. Phys.* **2000**, *113*, 9901-9904.

(22) Martoccia D.; Willmott P. R.; Brugger T.; Björck M.; Günther S.; Schlepütz C. M.; Cervellino A.; Pauli S. A.; Patterson B. D.; Marchini S.; Winterlin J.; Moritz W.; Greber T. *Phys. Rev. Lett.* **2008**, *101*, 126102.